TORQUE AND FORCE RESULTING FROM ECCENTRICITY IN OSCILLATION

NICK DERR, ALEX ZHAO

Abstract. The self-alignment and organization of small objects in fluids is important in many contexts including biology [17, 9], robotics [4], and medicine [3]. In laminar Stokes flow, viscous forces dominate, and Purcell's theorem forbids time-average steady flow as a result of oscillation. In turbulent flow, inertial forces dominate. At intermediate Reynolds numbers, not one of viscous or inertial forces can dominate the other. A number of recent works have investigated steady flows as a result of micro-oscillation in simple systems at intermediate Reynolds numbers. Here, we extend previous work and analyze the micro-oscillation behavior of fluid in a 2D circular domain, forced around two ellipses fixed in position. A perturbation analysis decomposes the problem into a series of linear problems, which are solved using the finite element method in complex numbers. The force and torque on each ellipse is computed with various geometric positions and Reynolds numbers Re. We find that in the single-ellipse case, the torque is sinusoidal in angular orientation, and also approximately proportional to Re, so angular orientation aligns perpendicular to the direction of oscillation. In the double-ellipse case, several local effects in the single-ellipse case are preserved. Furthermore, the change in the torque of one ellipse is also sinusoidal in the angular orientation of the other ellipse and proportional to Re, as well as being independent of the orientation of the one ellipse.

1. Introduction and Motivation

The self-alignment and organization of small objects in fluids is important in many contexts including biology [17, 9], robotics [4], and medicine [3]. Self-aligning objects can assemble into regular arrays and structures for the purposes of building construction, nano-sized medicine delivery, membrane construction, manufacturing, and more [4, 25]. The small length scales of these objects correspond to small values of the Reynolds number Re, a dimensionless measure of the relative importance of inertial as opposed to viscous forces. The Stokes equations resulting from small Reynolds numbers describe time-reversible viscous flows, so reciprocal motions yield no time-averaged motion, the so-called scallop theorem [20]. As a result, low-Re non-reciprocal action, such as bacteria cilia and spermatozoa tails [23, 19], has been studied in great detail.

On the other hand, at large length scales, corresponding to large Reynolds numbers, inertial forces dominate. Newton's third law allows swimmers to propel themselves forward by pushing fluid backwards. A large swimmer such as a fish can use reciprocal

Date: March 15, 2024.

Key words and phrases. steady streaming, perturbation, FEM, near-ellipses.

motion, e.g. kicking its tail, to propel itself, and swimming has been well studied in this regime as well [9].

If the Reynolds numbers are intermediate, however, viscous and inertial forces are comparable, and neither can be neglected. The case of a single sphere in oscillating fluid has been studied in all three of these cases. In the limit of small and large Reynolds numbers, expansions can be made in Re or Re^{-1} that simplify analysis by replacing a term from the Navier-Stokes equations [21]. For intermediate Re numbers, however, neither component can be omitted. In general, such a system has been shown to give rise to a leading-order oscillating flow. After taking a time average, this leading-order oscillating flow will cancel out, yielding a second-order steady flow [22]. This phenomenon, steady streaming, is also referred to in the literature as acoustic streaming or microstreaming.

It has been reported that within a viscous boundary layer, fluid is drawn towards the poles and subsequently ejected along the equator, whereas outside of this boundary layer, fluid is transported in the opposite direction through a Reynolds stress [21]. Additional experimental [18] and numerical [2] research have verified and further examined the flows resulting from this setup.

There has been increasing interest in the interaction between a number of small spheres in oscillating fluid. In 2002, [24] reported small spheres forming regular hexagonal lattices in a vertically vibrated 3D glycerol-water cell. In the same year, [26] reported experiments where small spheres undergoing sinusoidal vibrations formed equally spaced chains in a shallow, 2D water-filled cell. Chain formation of spheres in oscillation was further studied in [11]. In an effort to understand these many-sphere interactions, the induced forces on two spheres oscillating at intermediate Reynolds numbers have been studied experimentally and numerically by [12] and [7].

Previous study has primarily focused on rotationally symmetric spheres; even when ellipsoids were the focus, such as in [1], the geometric setup was assumed to be axisymmetric. Our goal is to extend the work of [7] and [12] by examining the role of asymmetry in the alignment of the angular orientations of two near-circles, or ellipses, in oscillating fluid. The work of [7] conjectures that steady streaming will act to align such objects perpendicular to the direction of oscillation, and our results are consistent with this prediction. We compute the induced torques contributed by eccentricity to determine the stable equilibrium of ellipse orientation in our geometric setup.

In the case of the problem of a collection of spherical beads oscillating in fluid, by examining the interaction between a pair of spheres, [12] established that the beads will arrange themselves in a chain perpendicular to the direction of oscillation. We aim to understand the direction of orientation of the beads in this chain if they were asymmetric, i.e. they were near-spheres instead of perfect spheres. Furthermore, we address the possibility of holding a single bead in a fixed orientation and thereby influencing the alignment of other beads in the chain. Applications for this include better understanding of the self-assembly of asymmetric, oblong, or even rod-like beads in

oscillating fluid, as well as the potential for the orientation of one such object to control the orientation of an array of other objects.

We would typically use freely moving circles and constrain their motion using the induced force from the surrounding fluid via Newton's third law. Rather than solving for freely moving objects, we fix the ellipses and calculate induced forces and torques in order to find the equilibrium configuration where these vanish.

As a notational note, we use bolded symbols for vector and tensor functions and values, and unbolded symbols for scalar functions and values. We also use $\Re$ to denote real parts of complex values.

In Section 2 we introduce the model system, variables, parameters, and equations. We treat the problem analytically, decomposing it into a series of linear problems using a series expansion whose derivation is detailed in Appendix A. We also introduce the expressions used to compute torque and force, derived in Appendix B. In Section 3 we introduce the finite element method used to solve each linear problem, and our solution procedure. In Section 4, we solve the single-ellipse case numerically. We find that in the case of a single sphere, the ellipse will always align perpendicular to the direction of oscillation, as predicted by [7]. Specifically, the torque is sinusoidal as a function of the angular orientation, and is also approximately proportional to Re. Furthermore, as Re increases the boundary layer thins. Finally, in Section 5, we present numerical results for the double-ellipse problem. We qualitatively compare our model to the plotted survey of velocity field flows and forces in [7] and [21], and demonstrate several instances of corroborating symmetry. We then survey the leading-order torques contributed by eccentricity at the locations of force equilibrium. Our double-ellipse numerical findings indicate that at intermediate Reynolds numbers, the angular displacement of one ellipse does not have a significant impact on the torque experienced by the other ellipse, so holding a single ellipse in a fixed angular position will not have a significant controlling effect on the other ellipse. This change in the torque of one ellipse is also found to be sinusoidal in the angular orientation of the other ellipse. Finally, just as in the single-ellipse case, the stable orientation is $\frac{\pi}{2}$, as [7] predicted.

2. Model System

In this section we set up the preliminary analysis for our physical model. We first introduce a model of our system in Subsection 2.1. In Subsection 2.2 we simplify this model via non-dimensionalization. In Subsection 2.3 we expand our solution in two small parameters corresponding to eccentricity and oscillation magnitude, and obtain a series of four coupled linear problems. Finally, in Subsection 2.4 we derive expressions for the forces and torques on the ellipses.

2.1. **System parameters.**

Our model system consists of two congruent ellipses fixed in place in a rigid two-dimensional circular domain of incompressible fluid. The fluid has density ρ and viscosity μ. We denote the fluid domain by Ω and the domain of

ellipse k by Ω_k for $k = 1, 2$. We denote the boundaries of these domains by $\partial\Omega$ and $\partial\Omega_k$, respectively. The fluid velocity is oscillating in the x-direction at the boundary of the domain. We wish to compute the fluid velocity $\boldsymbol{u}(\boldsymbol{x}, t)$ and fluid pressure $p(\boldsymbol{x}, t)$ in terms of the two-dimensional position vector $\boldsymbol{x}$ and the time scalar t.

Our geometric setup is depicted in Figure 1. The circular domain has diameter S, and the oscillation has magnitude U and frequency ω. The center of each of the ellipses is distance D from the center of the domain. Following [21], we assume $R \gg U/\omega$ so that the distance travelled by the oscillation in one cycle is much smaller than the size of the ellipse. We introduce ellipses with semimajor axis $R + R_\Delta$ and semiminor axis $R - R_\Delta$, where $R \gg R_\Delta$. Because the two ellipses are fixed in place, their density is not relevant to our analysis.

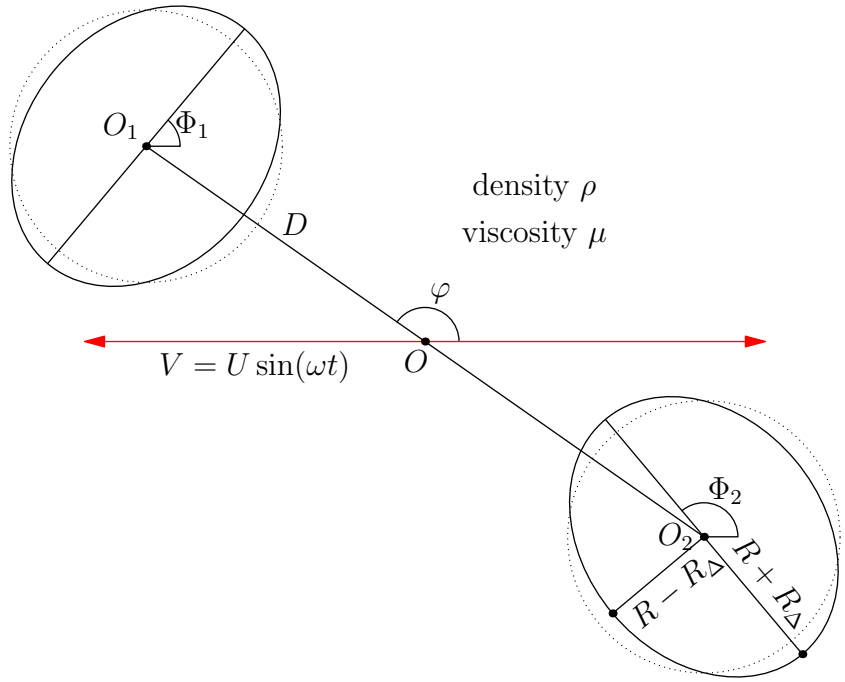

FIGURE 1. Schematic of geometric setup. Two near ellipses with semimajor and semiminor axes length $R + R_\Delta$ and $R - R_\Delta$, respectively, with centers a distance D from the system's center of mass. The circles with radius R these ellipses are perturbed from are shown in dashed lines. The angle φ is the angular position of the two ellipses relative to the oscillation direction, while the angles Φ_1, Φ_2 are the angular positions of the major axes of Ω_1, Ω_2, respectively, relative to the oscillation direction.

The centers of the ellipse domains Ω_k we denote with O_k. We fix the center of the domain O at the center of mass of the two ellipses, the midpoint of O_1 and O_2. The

angle between the line $\overline{O_1O_2}$ and the horizontal we denote by φ. The angle between the major axis of Ω_k and the horizontal we denote by Φ_k.

2.2. **Nondimensionalized system.** We introduce characteristic length, frequency, and density scales R, ω, and ρ. Now, the fluid system is reduced to two parameters. Firstly, we have the Reynolds number

$$\mathrm{Re} = \frac{\rho R^2 \omega}{\mu}. \tag{2.1}$$

Secondly, we have the magnitude of oscillation relative to the length scale, $\varepsilon_1 = \frac{U}{R\omega}$, which we assume to be small following [8] and consequently [5]. The frequency of the oscillation is now 1.

The physical geometry of the system is reduced to six parameters. We have $L = \frac{S}{R}$, the non-dimensionalized diameter of the domain, $\varepsilon_2 = \frac{R_\Delta}{R}$, the small parameter describing the ellipses' perturbation from a perfect circle, and $K = \frac{D}{R}$, the distance from O_k to O. The semimajor and semiminor axes of the ellipses now have lengths $1+\varepsilon_2$ and $1-\varepsilon_2$, respectively. The angular parameters φ, Φ_1, Φ_2 were dimensionless to begin with, so they remain the same.

On the boundary of the domain the fluid must satisfy

$$\boldsymbol{u}(\boldsymbol{x}, t) = \varepsilon_1 \sin(t)\vec{\boldsymbol{x}} \tag{2.2}$$

for $\boldsymbol{x} \in \partial\Omega$. Because the ellipses are fixed in place, the fluid must be stationary on the boundary of the sphere, i.e. $\boldsymbol{u}(\boldsymbol{x}, t) = \boldsymbol{0}$ for $\boldsymbol{x} \in \partial\Omega_k$.

We assume the fluid is Newtonian and incompressible, so the fluid satisfies the Navier-Stokes equations

$$\mathrm{Re}\left(\frac{\partial \boldsymbol{u}}{\partial t} + \boldsymbol{u}\cdot\boldsymbol{\nabla}\boldsymbol{u}\right) = -\boldsymbol{\nabla}p + \boldsymbol{\nabla}^2\boldsymbol{u}, \quad \boldsymbol{\nabla}\cdot\boldsymbol{u} = 0. \tag{2.3}$$

2.3. **Series expansion.** The fluid velocities scale with the oscillation magnitude $\varepsilon_1 \ll 1$, suggesting a series expansion in ε_1 as made in [5]. Here we are interested in the effect of the eccentricity on the fluid flow, so we simultaneously expand in ε_2.

We ignore all terms with no effect on the $\mathscr{O}(\varepsilon_1^2\varepsilon_2)$ steady flow resulting from eccentricity. Motivated by the expansions used in [8] and subsequently [5], we adopt the ansatz

$$\boldsymbol{u}(\boldsymbol{x}, t) = \varepsilon_1 e^{it}(\hat{\boldsymbol{u}}_0 + \varepsilon_2\hat{\boldsymbol{u}}_1) + \varepsilon_1^2(\bar{\boldsymbol{u}}_0 + \varepsilon_2\bar{\boldsymbol{u}}_1). \tag{2.4}$$

A detailed derivation can be seen in Appendix A.

Here, we take the real parts of any complex exponentials. The magnitude and argument of the complex vector field $\hat{\boldsymbol{u}}$ correspond to the leading-order oscillating flow magnitude and phase shift, respectively. If $\hat{\boldsymbol{u}} = re^{i\theta}$, taking the real part of $e^{it}\hat{\boldsymbol{u}} = e^{it}(re^{i\theta})$ yields $r\cos(t+\theta)$, where r is the magnitude and θ is the phase shift.

We obtain a similar ansatz for the pressure scalar field

$$p(\boldsymbol{x}, t) = \varepsilon_1 e^{it}(\hat{p}_0 + \varepsilon_2 \hat{p}_1) + \varepsilon_1^2(\bar{p}_0 + \varepsilon_2 \bar{p}_1). \tag{2.5}$$

Substituting the ansatz into the Navier-Stokes Equation (2.3) and matching coefficients yields a series of linear differential equations, the derivation for which is in Appendix A. The equations describing the leading-order terms $\hat{\boldsymbol{u}}_0$ and $\bar{\boldsymbol{u}}_0$ are

$$\left(\boldsymbol{\nabla}^2 - i\,\mathrm{Re}\right)\hat{\boldsymbol{u}}_0 = \boldsymbol{\nabla}\hat{p}_0, \qquad \boldsymbol{\nabla}\cdot\hat{\boldsymbol{u}}_0 = 0 \tag{2.6}$$

$$\boldsymbol{\nabla}^2\bar{\boldsymbol{u}}_0 = \boldsymbol{\nabla}\bar{p}_0 - \boldsymbol{\nabla}\cdot\boldsymbol{R}_0, \qquad \boldsymbol{\nabla}\cdot\bar{\boldsymbol{u}}_0 = 0 \tag{2.7}$$

where $\boldsymbol{R}_0 = -\frac{1}{2}\,\mathrm{Re}\,\hat{\boldsymbol{u}}_0 \otimes \hat{\boldsymbol{u}}_0^*$, and $\otimes$ denotes the vector outer product. The tensor field $\boldsymbol{R}_0$ can be interpreted as the Reynolds stress driving the steady flow without eccentricity $\bar{\boldsymbol{u}}_0$. This Reynolds stress arises from the convective term $\boldsymbol{u}\cdot\boldsymbol{\nabla}\boldsymbol{u}$ in the Navier-Stokes Equation (2.3) [5, 7]. These equations match Equations 2.13-14 in [5] as expected, because $\hat{\boldsymbol{u}}_0$ and $\bar{\boldsymbol{u}}_0$ are the flows resulting from no eccentricity.

The equations describing the flows $\hat{\boldsymbol{u}}_1$ and $\bar{\boldsymbol{u}}_1$ resulting from eccentricity are

$$\left(\boldsymbol{\nabla}^2 - i\,\mathrm{Re}\right)\hat{\boldsymbol{u}}_1 = \boldsymbol{\nabla}\hat{p}_1, \qquad \boldsymbol{\nabla}\cdot\hat{\boldsymbol{u}}_1 = 0 \tag{2.8}$$

$$\boldsymbol{\nabla}^2\bar{\boldsymbol{u}}_1 = \boldsymbol{\nabla}\bar{p}_1 - \boldsymbol{\nabla}\cdot\boldsymbol{R}_1, \qquad \boldsymbol{\nabla}\cdot\bar{\boldsymbol{u}}_1 = 0 \tag{2.9}$$

where $\boldsymbol{R}_1 = -\frac{1}{2}\,\mathrm{Re}\,\hat{\boldsymbol{u}}_0 \otimes \hat{\boldsymbol{u}}_1^*$. Once again, $\boldsymbol{R}_1$ can be interpreted as the Reynolds stress driving $\bar{\boldsymbol{u}}_1$ arising from the convective term $\boldsymbol{u}\cdot\boldsymbol{\nabla}\boldsymbol{u}$ and the two terms $\varepsilon_1\hat{\boldsymbol{u}}_0, \varepsilon_1\varepsilon_2\hat{\boldsymbol{u}}_1$.

2.4. **Force and torque.** After determining the vector velocity field $\boldsymbol{u}$ and the scalar pressure field p, we can compute the time-averaged torque and force exerted on the ellipses. The leading-order terms $\hat{\boldsymbol{u}}_0$ and $\hat{\boldsymbol{u}}_1$ are oscillatory and will vanish over a time-average. Furthermore, when the ellipses are in equilibrium position, by [7] they will be in either axial position (parallel to the direciton of oscillation) or lateral position (perpendicular to the direction of oscillation), so by symmetry the terms $\hat{\boldsymbol{u}}_0$ and $\bar{\boldsymbol{u}}_0$ will contribute no torque. Thus we consider only the torques and forces contributed by the flow $\bar{\boldsymbol{u}}_1$ and corresponding pressure $\bar{p}_1$.

On the boundary of the ellipse domain Ω_k, the force exerted on Ω_k at that point is determined by $\boldsymbol{T}\cdot\boldsymbol{n}$, where $\boldsymbol{T}$ is the Cauchy stress tensor

$$\boldsymbol{T} = p\boldsymbol{I} + \frac{1}{2}\left(\boldsymbol{\nabla}\boldsymbol{u} + (\boldsymbol{\nabla}\boldsymbol{u})^T\right). \tag{2.10}$$

This follows the same approach used by [12] and [5], except that there is no perturbation caused by a moving boundary.

Accordingly, the vector-valued total force exerted on Ω_k is

$$\boldsymbol{F}_k = \int_{\partial\Omega_k} \boldsymbol{T}\cdot\boldsymbol{n}\,dS, \tag{2.11}$$

and the torque is

$$T_k = \boldsymbol{z} \cdot \int_{\partial\Omega_k} \boldsymbol{n} \times (\boldsymbol{T} \cdot \boldsymbol{n})\, dS. \tag{2.12}$$

Here we use the scalar value for torque, arrived at by taking the dot product of the cross product with $\boldsymbol{z}$, the out-of-plane normal unit vector. Naturally, the cross product's only nonzero component is the z-component.

We can decompose $\boldsymbol{F}_k$ and T_k using the same series expansion, yielding $\hat{\boldsymbol{F}}_{k,0}$, $\bar{\boldsymbol{F}}_{k,0}$, $\hat{\boldsymbol{F}}_{k,1}$ and $\bar{\boldsymbol{F}}_{k,1}$, and their corresponding torques. These forces and torques result from the flows $(\hat{\boldsymbol{u}}_0, \hat{p}_0)$, $(\bar{\boldsymbol{u}}_0, \bar{p}_0)$, $(\hat{\boldsymbol{u}}_1, \hat{p}_1)$ and $(\bar{\boldsymbol{u}}_1, \bar{p}_1)$ respectively.

The values $\hat{\boldsymbol{F}}_{k,0}, \hat{T}_{k,0}$ are the leading-order oscillating force and torque without eccentricity. Similarly, $\hat{\boldsymbol{F}}_{k,1}$ and $\hat{T}_{k,1}$ are the leading-order oscillating force and torque resulting from the presence of eccentricity. Because these are oscillating, they will vanish after taking a time-average. For this reason, following [7], we disregard these values in force and torque computations.

The values $\bar{\boldsymbol{F}}_{k,0}, \bar{T}_{k,0}$ are the leading-order *steady* force and torque without eccentricity, and $\bar{\boldsymbol{F}}_{k,1}, \bar{T}_{k,1}$ are the steady force and torque resulting from eccentricity. Thus the time-averaged force will be $\bar{\boldsymbol{F}}_{k,0}$. If $\bar{\boldsymbol{F}}_{k,0} = \boldsymbol{0}, \bar{T}_{k,0} = 0$ then the ellipses will remain in place, even if they were allowed to move freely. Thus at leading order, the stable equilibrium position of the ellipses is determined by a stable solution to $\bar{\boldsymbol{F}}_{k,0} = 0$.

From [7] we know that this force equilibrium position is a transverse configuration, so by symmetry $\bar{T}_{k,0} = 0$. Thus the ellipses will rotate with the second-order torque $\bar{T}_{k,1}$. Therefore, the ellipses will align with the angular orientation corresponding to a stable equilibrium $\bar{T}_{k,1} = 0$. The full expressions for $\boldsymbol{F}_{k,i}$ and $T_{k,i}$ can be found in Appendix B.

3. Numerical Procedure

In this section we describe the finite element analysis used to solve our linear problems. By combining consecutive solves, we can solve our series of coupled linear problems.

In Subsection 3.1 we introduce the weak form of the Brinkman equation and describe the library used to solve this weak form. Then in Subsection 3.2 we describe how the linear problems are solved in order, and the physical meaning of each of these solves.

3.1. **Finite element method.**

The dimensionless Brinkman equation can be expressed as

$$\left(\boldsymbol{\nabla}^2 - \alpha^2\right) \boldsymbol{u} = \boldsymbol{\nabla} p - \boldsymbol{f}. \tag{3.1}$$

Conventionally, this equation describes flow subject to a body force $\boldsymbol{f}$ in a porous region with drag coefficient $-\alpha^2$ [6]. If $\alpha = 0$ we obtain the classical Stokes equation. Using

test functions $\boldsymbol{v}$ and q corresponding to $\boldsymbol{u}$ and p, the weak form of Equation (3.1) is

$$\int_\Omega \left(\langle \boldsymbol{\nabla u}, \boldsymbol{\nabla v} \rangle + \alpha^2 (\boldsymbol{u} \cdot \boldsymbol{v}) - (\boldsymbol{\nabla} \cdot \boldsymbol{v}) p \right) dS = \int_\Omega \boldsymbol{v} \cdot \boldsymbol{f} \, dS, \quad \int_\Omega q (\boldsymbol{\nabla} \cdot \boldsymbol{u}) \, dV = 0. \tag{3.2}$$

Here $\langle \cdot, \cdot \rangle$ denotes the tensor inner product.

We now discretize our domain into triangular elements using the Frontal-Delauney meshing algorithm from the `gmsh` library [10]. Two sample meshes used to solve the 1-ellipse and the 2-ellipse cases are displayed in Figure 2. These are the meshes used to generate the flow field visualizations in Subsection 4.1 and Subsection 5.1.

(A) (B)

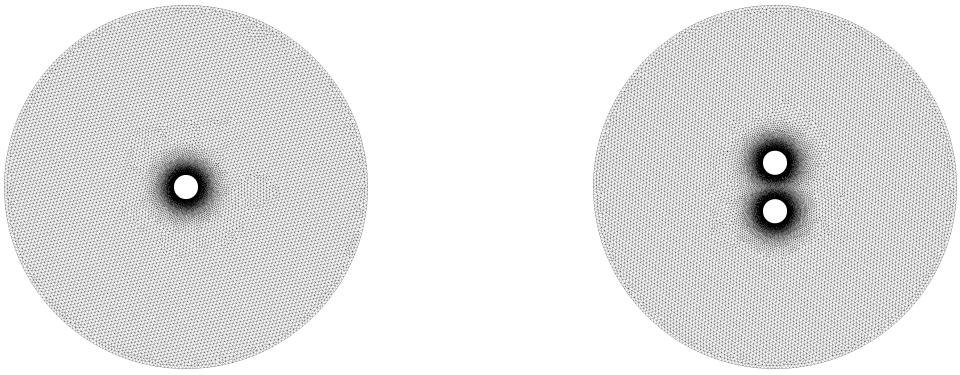

FIGURE 2. Two of the meshes used in our torque and force computations. We vary the distance of the circles from the center to generate different meshes for force computations.

On each element, for both $\boldsymbol{u}$ and p we use Lagrange polynomial functions. The vector field $\boldsymbol{u}$ is represented by degree 2 vector-valued Lagrange functions, and the scalar field p is represented by degree 1 scalar-valued Lagrange functions. Our solution space will be piecewise combinations of these. We are solving for the discretized approximation $\boldsymbol{u}^h$ and p^h on their respective meshes.

We use the distributed-memory version of the SuperLU library and PETSc library for scientific computation to directly solve the resulting matrix-vector problem [16, 15]. Intermediate terms are computed and interpolated using the UFL form language via DolfinX [13, 14]. In the solving process, we introduced terms $\varepsilon \approx 10^{-12}$ on the right-hand side of Equation (3.2) for regularization purposes.

3.2. **Solution procedures.** We wish to solve the system of equations eqs. (A.34) to (A.41).

The first problem Equation (2.6) describes the leading-order oscillatory flow disregarding eccentricity. The second problem Equation (2.7) describes the leading-order steady time-averaged flow disregarding eccentricity. The third problem Equation (2.8) describes the leading-order oscillatory flow contributed by eccentricity. The last problem Equation (2.9) describes the time-averaged steady flow contributed by eccentricity.

We solve these four problems in order, and arrive at four time-independent flows: $(\hat{\boldsymbol{u}}_0, \hat{p}_0), (\bar{\boldsymbol{u}}_0, \bar{p}_0), (\hat{\boldsymbol{u}}_1, \hat{p}_1), (\bar{\boldsymbol{u}}_1, \bar{p}_1)$. Once previous flows are computed, we substitute them into subsequent problems. Each problem will be of the form Equation (3.1), so we use the finite element procedure described in Subsection 3.1.

Finally, we integrate our discretized solutions on the mesh to compute the forces and torques for each flow on the two circles, according to the expressions in Subsection 2.4.

4. Single-ellipse Numerical Results

Applying the methods described in Section 3, we solve for $\hat{\boldsymbol{u}}_0, \bar{\boldsymbol{u}}_0, \hat{\boldsymbol{u}}_1, \bar{\boldsymbol{u}}_1$ in that order for the single-ellipse problem.

4.1. **Single-ellipse flow fields.**

Firstly, we present flow field plots, with velocity streamlines and a vorticity colormap.

All the flows depicted in Figure 3 are independent of the eccentricity of the near spheres, and so the orientation of the major axis is not shown. The flows were solved in a circular domain of diameter 30, then cropped to a 16×16 box and plotted.

The plots for $\Phi = \frac{\pi}{2}$ are excluded here, because adding $\frac{\pi}{2}$ to Φ is equivalent to sign flipping ε_2, so $\hat{\boldsymbol{u}}_1$ and $\bar{\boldsymbol{u}}_1$ simply sign flip. This can be confirmed with the $\Phi = \frac{\pi}{2}$ plot shown in our supplement.

We first analyze the flows $\hat{\boldsymbol{u}}_0$ and $\bar{\boldsymbol{u}}_0$ without eccentricity. As seen in Figure 3, the sign of the vorticity around the circle boundary, as well as the qualitative arrangement of the double boundary layer, is invariant of Re. However, as Re increases, boundary layers thin and become more concentrated. As Re gets sufficiently large, i.e. at $\mathrm{Re} = 10$ for $\hat{\boldsymbol{u}}_0$ and at $\mathrm{Re} = 100$ for $\bar{\boldsymbol{u}}_0$, a second vortex appears. Notice that in the top-right corner, in Figures 3c and 3e the flow is clockwise, but in Figure 3f the flow is clockwise.

As Re increases, boundary behavior becomes stronger, flow in the bulk becomes weaker, and the secondary vortex comes closer to the origin, as predicted by [21]. Now we can introduce eccentricity into our analysis, by examing the flows $\hat{\boldsymbol{u}}_1$ and $\bar{\boldsymbol{u}}_1$.

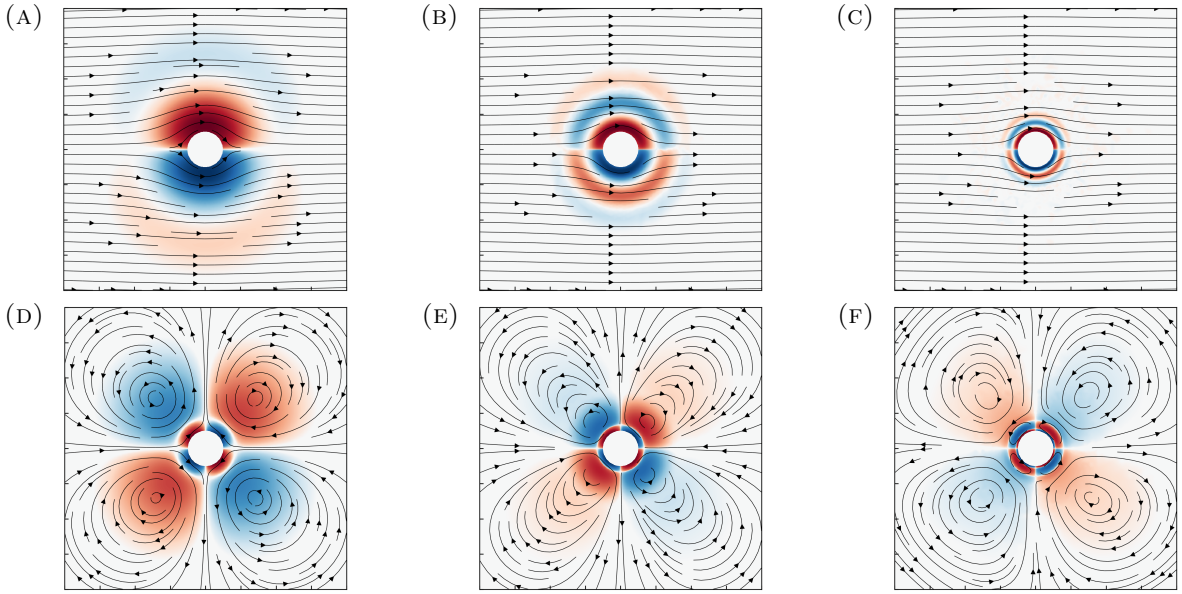

FIGURE 3. Array of plots of vorticity and velocity streamlines for single-ellipse flows without eccentricity. Three columns correspond to $\mathrm{Re} = 1, 10, 100$ respectively. Two rows correspond to $\hat{\boldsymbol{u}}_0$ and $\bar{\boldsymbol{u}}_0$ respectively.

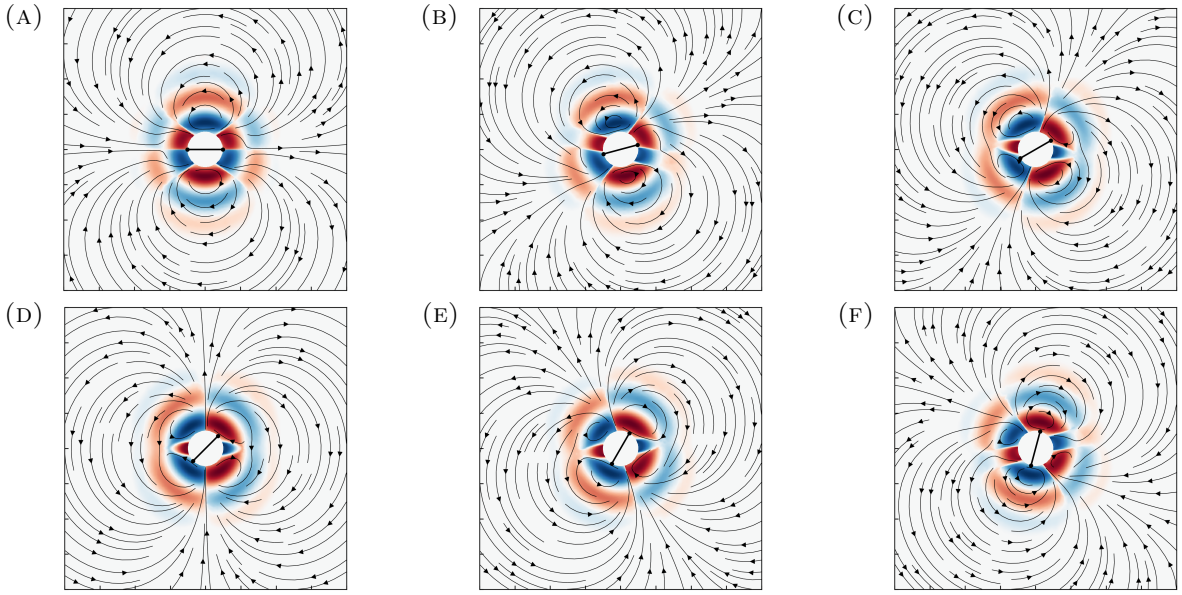

FIGURE 4. Array of plots at $\mathrm{Re} = 10$ of vorticity and velocity streamlines of the oscillating flow resulting from eccentricity $\hat{\boldsymbol{u}}_1$. From Figures 4a to 4f Φ is incremented $\frac{\pi}{12}$ radians at a time, from $\Phi = 0$ to $\Phi = \frac{5\pi}{12}$.

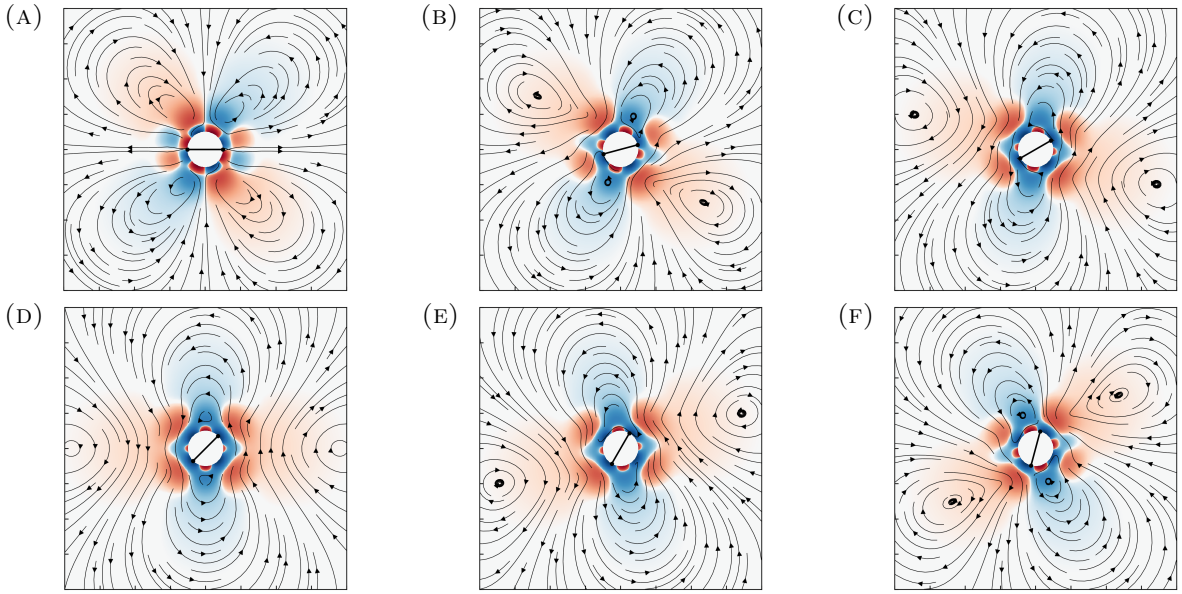

FIGURE 5. Array of plots at $\mathrm{Re} = 10$ of vorticity and velocity streamlines of the steady flow resulting from eccentricity $\bar{\boldsymbol{u}}_1$. From Figures 5a to 5f Φ is incremented $\frac{\pi}{12}$ radians at a time, from $\Phi = 0$ to $\Phi = \frac{5\pi}{12}$.

As seen in Figures 4 and 5 respectively, the vorticity in the neighborhood of the ellipse has a characteristic 3-periodicity in $\hat{\boldsymbol{u}}_1$ and 4-periodicity in $\bar{\boldsymbol{u}}_1$. The 3- and 4-periodicity for $\hat{\boldsymbol{u}}_0$ and $\bar{\boldsymbol{u}}_0$, respectively, is created by the sign changes in the $\cos(2\theta - 2\Phi)$ term in the boundary condition. Notice that sign flips in the periodicity are near locations satisfying $\cos(2\theta - 2\Phi) = 0$. At these locations on the the boundary we necessarily have $\hat{\boldsymbol{u}}_1 = \bar{\boldsymbol{u}}_1 = \mathbf{0}$.

4.2. **Single-ellipse torques.** Finally, we move on to examining torques on the ellipse for various values of Φ and Re.

Examining Equation (A.36), we see that $\bar{\boldsymbol{u}}_0$ is driven by the Reynolds stress $\frac{1}{2}\,\mathrm{Re}(\hat{\boldsymbol{u}}_0 \cdot \boldsymbol{\nabla}\hat{\boldsymbol{u}}_0^*)$, so we expect $\bar{\boldsymbol{u}}_0$ to be approximately proportional to Re. Then from Equations (A.40) and (A.41) we see that $\bar{\boldsymbol{u}}_1$ is driven by a Reynolds stress and boundary condition proportional to Re, so we expect the torque to be proportional to Re as well. Thus, we scaled the coloring in this plot by $\log \mathrm{Re}$, and scaled the torques by Re.

As seen in Figure 6, the torque resulting from $\bar{\boldsymbol{u}}_1$ is sinusoidal in Φ. The close coincidence of the scaled plots demonstrates that the torques scale with Re.

The torque $\bar{\boldsymbol{u}}_1$ equals 0 at two points, $\Phi = 0$ and $\Phi = \frac{\pi}{2}$. As conjectured in the conclusion of [7], the torque is increasing at $\Phi = 0$ and decreasing at $\Phi = \frac{\pi}{2}$, i.e. the only stable equilibrium for angular orientation is at $\Phi = \frac{\pi}{2}$.

We will continue to study torques in the double-ellipse case in Subsection 5.3.

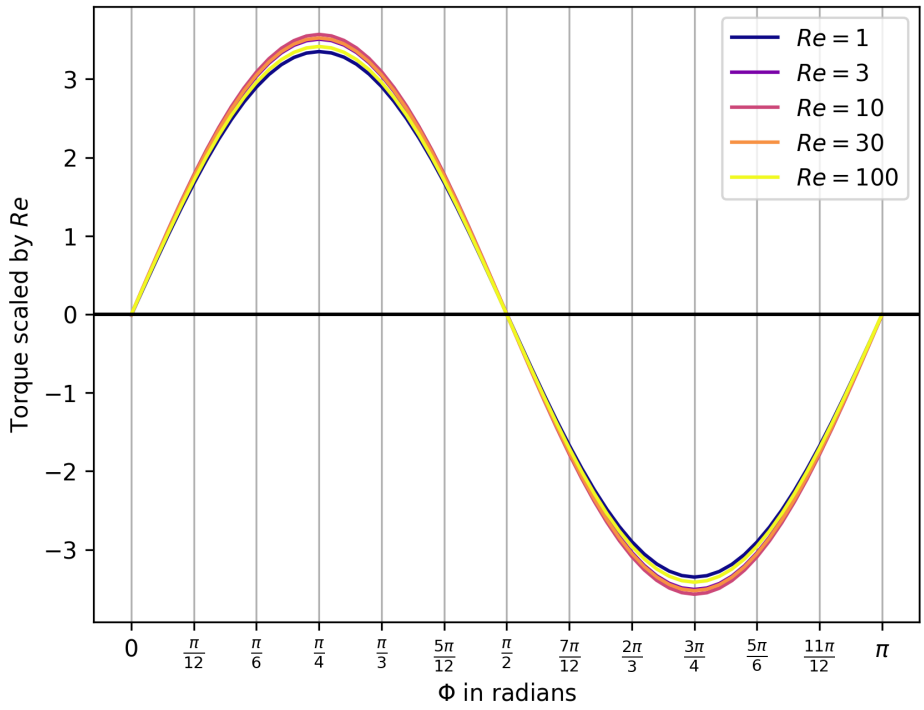

FIGURE 6. Plot of eccentricity-induced steady torques as a function of Φ, for various Re values. These plots have been scaled by Re.

5. Double-ellipse Numerical Results

Now that we have completed a numerical analysis of the single-ellipse case in Section 4, we move on to numerical results for the double-ellipse case.

Our results include flow field visualization in Subsection 5.1, force and equilibrium analysis in Subsection 5.2, and finally the torque and orientation analysis in Subsection 5.3.

We find that most of the effects localized to the ellipse that were explored in Section 4 still hold in the double-ellipse case. We qualitatively corroborate our force computations with [7]. Finally, we explore the torques in the double-ellipse case. We find that the torque of one ellipse is sinusoidal in the angular orientation of that ellipse, while the perturbation from the orientation of the other ellipse is also sinusoidal in that ellipse's angular orientation, albeit approximately one order of magnitude smaller. In addition, the equilibrium position from the single-ellipse case holds here, with both ellipses orienting perpendicular to the direction of oscillation, parallel to the direction of alignment.

5.1. **Double-ellipse flow fields.** Before examining the force and torque induced on these ellipses, we wish to understand the qualitative nature of the flows varied across the parameter space.

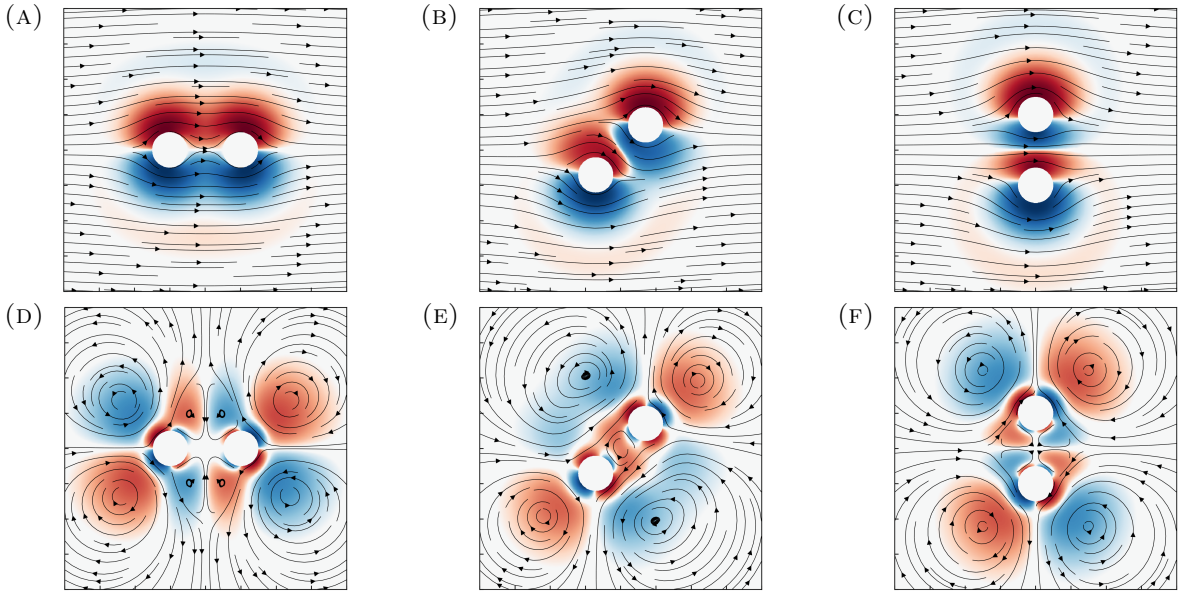

FIGURE 7. Array of plots of vorticity and velocity streamlines at $\mathrm{Re} = 1$. Three columns correspond to $\varphi = 0, \frac{\pi}{4}, \frac{\pi}{2}$ respectively. Two rows correspond to $\hat{\boldsymbol{u}}_0$ and $\bar{\boldsymbol{u}}_0$ respectively.

Figure 7 is an array of plots with velocity flow streamlines and log-scaled vorticity colormaps for various φ values at $K = 2$ and $\mathrm{Re} = 1$. All the flows depicted in Figure 7 are independent of the eccentricity of the near spheres, and so the orientation of the major axis is not shown. As in Subsection 4.1, these flows were cropped to a 16×16 box before being plotted. We used $\mathrm{Re} = 1$, with a separation distance of 2, corresponding to $K = 2$.

Here, columns are associated with the angular position φ. The first row is the leading-order oscillatory flow $\hat{\boldsymbol{u}}_0$, and the second row is the leading-order steady flow $\bar{\boldsymbol{u}}_0$.

Just as in Subsection 4.1, the streamline plots of Figures 7a to 7c show fluid flow in the direction of oscillation uniformly throughout the domain, regardless of φ.

We can qualitatively corroborate these plots with existing results about 2D and 3D steady streaming. The steady flow moves fluid from the poles (the left and right ends of the circles) to the equator (the top and bottom ends of the circles), as predicted by [21]. The vortex rings in the steady flow also match those predicted by [21]. Furthermore, the streamline plots of Figures 7d to 7f qualitatively match those found in [7]; note that the colormaps in [7] refer to the pressure field, unlike our plots.

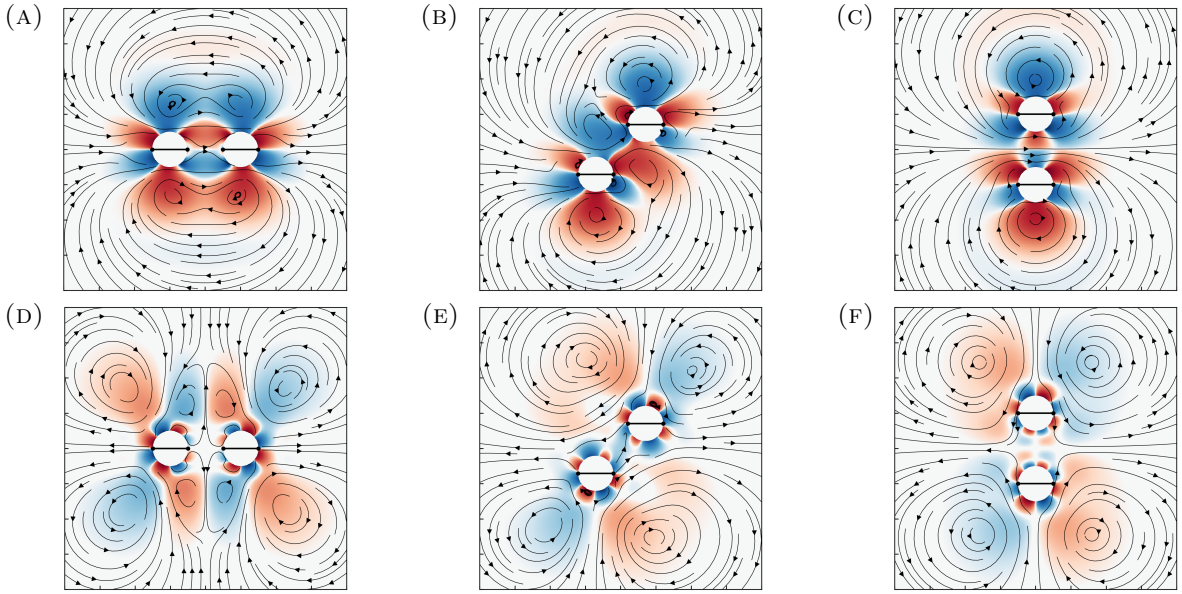

FIGURE 8. Three columns correspond to $\varphi = 0, \frac{\pi}{4}, \frac{\pi}{2}$ respectively at $\mathrm{Re} = 1$. Two rows correspond to $\hat{\boldsymbol{u}}_1$ and $\bar{\boldsymbol{u}}_1$ respectively, with $\Phi_1 = \Phi_2 = 0$, as indicated by the black bar.

Having reviewed the nature of flows around symmetric objects, we turn to those around asymmetric objects. The plots in Figure 8 show the flows contributed by eccentricity. The orientation of the major axis is indicated by the black bar across the ellipses. These plots exhibit symmetry across the center of mass, as well as left-right and top-down symmetry in the cases of $\varphi = 0$ and $\varphi = \pi$, as expected.

Just as in the single-ellipse case as studied in Subsection 4.1, these flows exhibit a characteristic local 3-periodicity and 4-periodicity. This correspondence of local characteristics is expected, because as the position gets closer to one ellipse, the relative impact of the other ellipse rapidly diminishes.

Furthermore, the arrangement of the signs of vorticity near the circle boundary are consistent across different φ values, with positive vorticity described approximately by the region $\theta \in (0, \frac{\pi}{4}) \cup (\frac{3\pi}{4}, \pi) \cup (\frac{5\pi}{4}, \frac{7\pi}{4})$. This consistency is expected, because at increasingly small distances to one ellipse, the effect of the relative position of the other circle should rapidly diminish.

As further confirmation, we can examine the case $\varphi = \pi$ in the same geometric positions. Similarly to our discussion in Subsection 4.1, adding $\frac{\pi}{2}$ to Φ_i is equivalent to flipping the sign of ε_2, keeping the same geometric setup otherwise. Then it is apparent that $\hat{\boldsymbol{u}}_0$ and $\bar{\boldsymbol{u}}_0$ will sign-flip. This flow survey is included in our supplement.

Finally, Figure 9 depicts a survey of flows with $\Phi_1 = 0$ and $\Phi_2 = \frac{\pi}{2}$. Notice the new sign-flip behavior here; compared to the $\Phi_1 = \Phi_2 \in \{0, \frac{\pi}{2}\}$, the vorticity is now an even

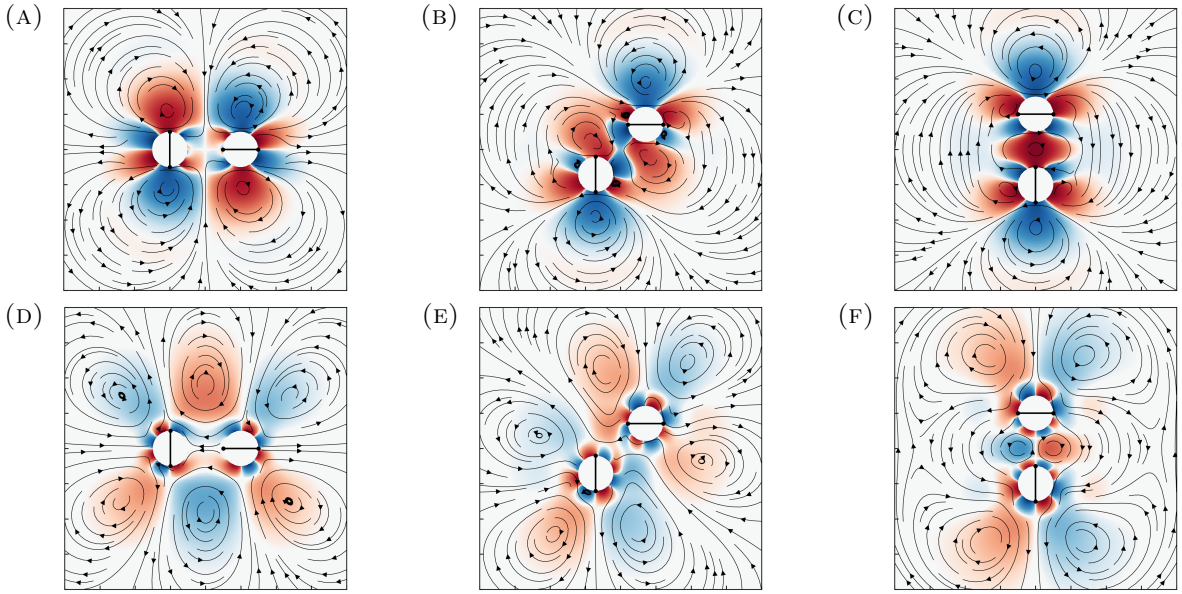

FIGURE 9. Three columns correspond to $\varphi = 0, \frac{\pi}{4}, \frac{\pi}{2}$ respectively at $\mathrm{Re} = 1$. Two rows correspond to $\hat{\boldsymbol{u}}_1$ and $\bar{\boldsymbol{u}}_1$ respectively, with $\Phi_1 = 0, \Phi_2 = \frac{\pi}{2}$, as indicated by the black bar.

function of position where it was an odd function before, and vice versa. This is because the geometric setup now has reflective symmetry instead of rotational symmetry.

We further study the effect of Φ_1 and Φ_2 on the fluid flow in Subsection 5.3.

5.2. **Double-ellipse force analysis.** After analyzing these flows qualitatively, we now analyze the resulting forces and torques on the ellipses numerically, and once again corroborate our model with existing results. We begin with the force.

The leading-order force on the ellipses is from $\bar{\boldsymbol{u}}_0$. Only when $\bar{\boldsymbol{F}}_0 = \boldsymbol{0}$ has the sphere reached equilibrium.

As stated in [7], at equilibrium, the circles are either in horizontal (axial) configuration, or vertical (lateral/transverse) configuration. In the case of unbounded fluid, the only stable equilibria are in the transverse configuration. More specifically, there is exactly one stable equilibrium in the transverse configuration, and there is at most one equilibrium in the axial configuration which is always unstable.

Figure 10 displays a force survey in the transverse configuration, and a plot of the equilibrium K value for various Reynolds numbers. We consider only the transverse configuration to restrict our analysis to stable equilibria.

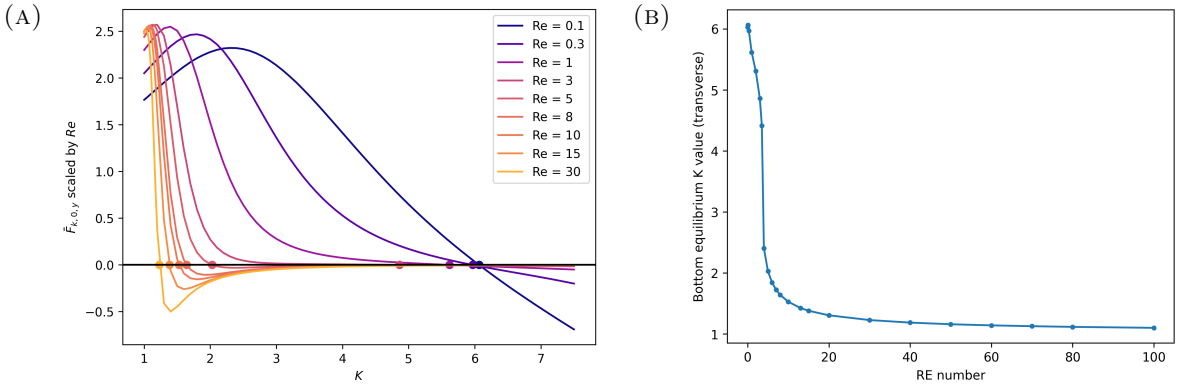

FIGURE 10. The left-hand plot is a survey of the force applied on each of the circles in the transverse direction varying with respect to K, for various values of Re. These have been scaled with Re. The right-hand plot is a graph of the K-value of the transverse configuration near equilibria with respect to Re.

As discussed in Subsection 4.2, we expect $\bar{\boldsymbol{u}}_0$ to scale approximately with Re, and consequently the force should also scale with Re. Indeed, these forces are of similar magnitude after scaling by Re, as seen at the left endpoints in Figure 10a.

These surveys qualitatively match results from [7]. Because this is Re-scaled, it is clear that larger Reynolds numbers exhibit larger forces than smaller Reynolds numbers, as originally found in [7].

Now we examine the force equilibrium position as a function of Re. We determined the equilibria positions in Figure 10b using a bisection search. The determined equilibrium positions correspond to x-intercepts in the force survey with a negative first derivative, signifying a stable equilibrium. These x-intercepts are marked on the x-axis in Figure 10a.

The left endpoint is Re $= 0.01$. The plot suggests that as Re $\to 0$ the equilibrium position converges. This can also be seen from several force functions having roots in the same vicinity in Figure 10a. As noted in [7] the equilibrium position should limit to ∞ as Re $\to 0$, but because of boundary effects the equilibrium K value stalls at approximately one third of the domain radius. Thus, this convergence should not be expected in the case of unbounded fluid.

The sharp drop in the equilibrium position in Figure 10b near Re $= 3.5$ is attributed to the flatness of the force as a function of K as seen in Figure 10a. The rapid change in equilibrium distance at approximately Re $= 5$ can be attributed to the stiff behavior of the force $F = F(K)$, as the function's derivative approaches zero as shown in Figure 10a. Specifically, the flat part of the function as a force of K yields a critical Re value where the equilibrium distance rapidly decreases.

Finally, as $\mathrm{Re} \to \infty$ we see the equilibrium K tending towards 1, corresponding to a separation distance of 0.

5.3. **Double-ellipse torques.** For the values of K, φ, Re such that the ellipses experience no force, we can examine their torques. We use the equilibrium positions of $\bar{\boldsymbol{F}}_{k,0}$ as shown in Figure 10b.

As discussed in Subsection 2.4, the rotation and alignment of the ellipses in these configurations is driven solely by $\bar{T}_{k,1}$. From henceforth, we abbreviate $\bar{T}_{k,1}$ by simply T_k.

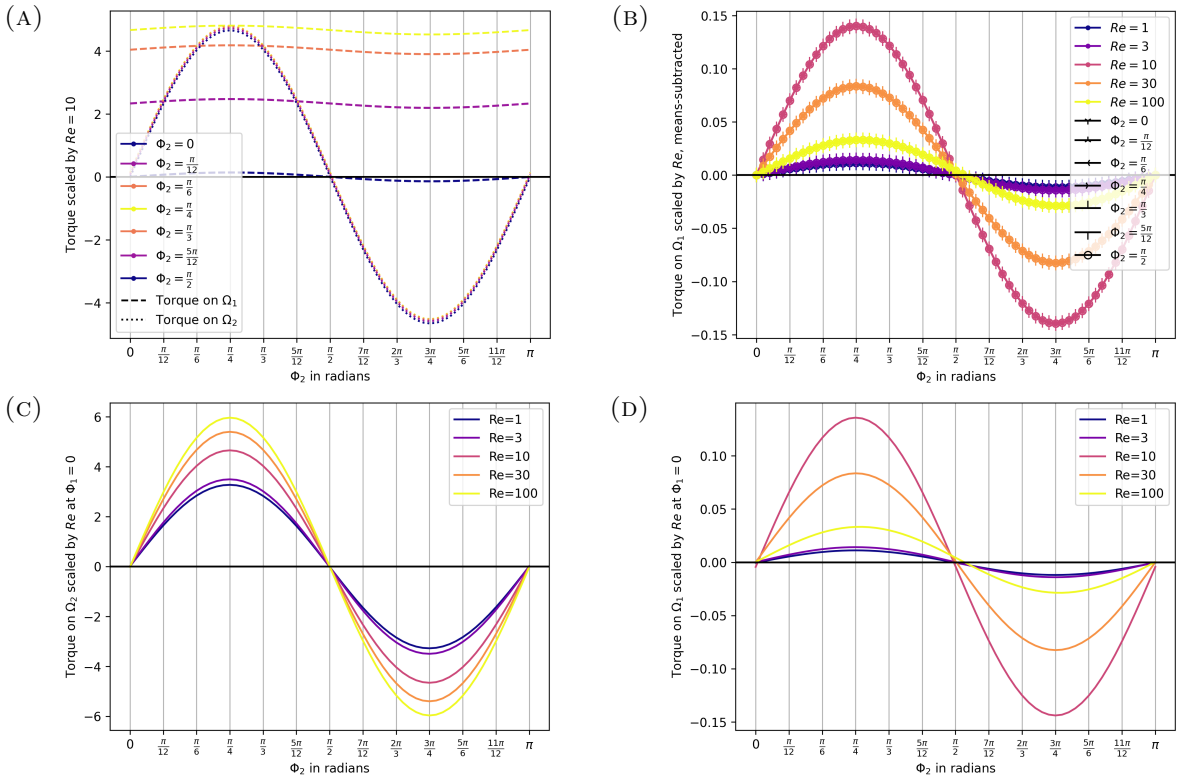

FIGURE 11. In all four plots, the x-axis is a survey over 60 values of Φ_2. Figure 11a is a survey of torques on Ω_1 and Ω_2 for various values of Φ_1. Figure 11b is a survey of the means-adjusted torques on Ω_1 for various values of Φ_1 and Re, with color and marker indicating the combination. Figure 11c plots the torques on Ω_2, i.e. a survey of the torque of one ellipse as a function of the orientation of that ellipse. On the other hand Figure 11d plots the torques on Ω_1, i.e. a survey of the torque of one ellipse as a function of the orientation of the other ellipse.

For $\mathrm{Re} = 1, 3, 10, 30$, and 100, we surveyed T_k for $\Phi_1 = \frac{n\pi}{12}$ for integer $0 \le n \le 6$ and a dense collection of $\Phi_2 \in [0, \pi)$. The plot for $\mathrm{Re} = 10$ is shown in Figure 11a; the

remainder are similar. Similarly to Figure 6 and Figure 10a, we scaled all torques by the Reynolds number, because $\bar{\boldsymbol{u}}_1$ scales approximately with Re.

We can make several corroborating symmetry observations. In Figure 11a, at $\Phi_1 = \Phi_2$, we obtain $T_1 = T_2$, as expected from symmetry across the center of the domain. Furthermore, $T_1 = T_2 = 0$ at $\Phi_1, \Phi_2 \in \{0, \frac{\pi}{2}, \pi\}$, as expected from left-right symmetry.

Furthermore, the stable equilibrium is demonstrated to always be at $\Phi_i = \frac{\pi}{2}$. As can be seen from the T_1 plots, if one of the circles is held at a non-equilibrium angle, the equilibrium position of the other circle will be only slightly perturbed.

For all four Reynolds numbers, we see that as Φ_2 varies, the value of T_2 varies much more than the value of T_1. Comparing amplitudes between Figure 11c and Figure 11d, the amplitude of the variation of T_1 is 0.02-0.05 times that of T_2, i.e. T_1 does not change much in response to change in Φ_2. Similarly, the value of T_2 barely changes as Φ_1 varies.

Thus, for Re $\in [1, 100]$, we conclude that the torques of the two circles are mostly independent of the others' position.

As seen from Figure 11b, the change in T_1 as a function of Φ_2 is sinusoidal. The markers for the same Re value all coincide, demonstrating that this change is independent of the current value of Φ_1. Thus, at leading order, the steady torque from eccentricity T_1 is a sum of two univariate sinusoidal functions, one with larger amplitude in Φ_1 and the other with smaller amplitude in Φ_2.

In conclusion, the orientation of a ellipse does not have a controlling effect on the torque induced on the other ellipse. After the two ellipse reach a point where the forces are 0, they will find a stable equilibrum when align themselves with their major axes perpendicular to the direction of oscillation. If one of their axes is aligned parallel to the direction of oscillation, that ellipse is in an unstable equilibrium.

6. Conclusion

In this work, the flow around two near-circles, or ellipses, in a circular domain subjected to a uniformly oscillating flow was analyzed using a series expansion. We expanded in two small parameters, the oscillation magnitude and the relative perturbation of the near-circles from perfect circles. Our series expansion yielded four pairs of velocity vector fields and pressure scalar fields, corresponding to the leading order oscillatory and steady flow without eccentricity, and the leading order oscillatory and steady flow induced by eccentricity.

We first analyzed the numerical solution to single-ellipse case, concluding that the stable orientation of a single ellipse is in the direction perpendicular to oscillation, as predicted by [7]. Furthermore, the torque is sinusoidal in the angular orientation Φ, and approximately proportional to Re.

Next, we analyzed the double-ellipse case with our solver. We first plotted the vorticity and streamlines of our flows, which qualitatively match similar results obtained by [7, 21].

We then surveyed the leading order force and equilibrium points without eccentricity by Reynolds number. The force scales with Re, and the equilibrium value for the distance of the center of the circle to the center of the domain K converges as $\mathrm{Re} \to 0$. However, As $\mathrm{Re} \to \infty$, this same equilibrium value for K limits to 1, corresponding to a separation distance of 0.

Finally, we surveyed the leading order torque contributed by eccentricity. Because the force equilibrium points are left-right symmetric, they have zero torque in the leading-order flows without eccentricity. Thus, we can analyze the torque in the steady flows contributed from eccentricity to determine the stable equilibrium of angular alignment.

Our numerical analysis determined that for various intermediate Reynolds numbers, the circles orient with both of their major axes pointing perpendicular to the direction of oscillation as predicted by [7], with an unstable equilibrium at the parallel orientation. Furthermore, the angular position of one circle did not have a significant effect on the torque experienced by the other circle. Specifically, at leading order, the torque on one circle is the sum of two univariate functions that are sinusoidal in each of the angular orientations. Extrapolating to a larger collection of ellipses or near spherical beads, after alignment into a chain perpendicular to the direction of oscillation as indicated by [11], the ellipses will orient with their major axis pointing in the same direction as the chain, perpendicular to the direction of oscillation, just as predicted by [7].

Extrapolating to the case of a chain of near spheres, we surmise that after alignment [7], the major axes of the ellipses will orient themselves perpendicular to the direction of oscillation, parallel to the chain. However, a single near sphere held in position does not have a controlling effect on the orientations of other near spheres.

Acknowledgements

We would like to thank the PRIMES-USA program at MIT Mathematics for making this research possible.

Appendix A. Ansatz Derivation and Series Expansion

We use the expansions

$$\boldsymbol{u} = \varepsilon_1 e^{it}(\hat{\boldsymbol{u}}_0 + \varepsilon_2 \hat{\boldsymbol{u}}_1 + \mathscr{O}(\varepsilon_2^2)) + \varepsilon_1^2(\bar{\boldsymbol{u}}_0 + \varepsilon_2 \bar{\boldsymbol{u}}_1 + \mathscr{O}(\varepsilon_2^2)) + \mathscr{O}(\varepsilon_1^3) \tag{A.1}$$

$$= \varepsilon_1 \left(\frac{e^{it}\hat{\boldsymbol{u}}_0 + e^{-it}\hat{\boldsymbol{u}}_0^*}{2} + \varepsilon_2 \frac{e^{it}\hat{\boldsymbol{u}}_1 + e^{-it}\hat{\boldsymbol{u}}_1^*}{2} \right) + \varepsilon_1^2(\bar{\boldsymbol{u}}_0 + \varepsilon_2 \bar{\boldsymbol{u}}_1) + \mathscr{O}(\varepsilon_2^2) + \mathscr{O}(\varepsilon_1^3), \tag{A.2}$$

$$p = \varepsilon_1 e^{it}(\hat{p}_0 + \varepsilon_2 \hat{p}_1) + \varepsilon_1^2(\bar{p}_0 + \varepsilon_2 \bar{p}_1) + \mathscr{O}(\varepsilon_1^3). \tag{A.3}$$

Both $\hat{\boldsymbol{u}} = \hat{\boldsymbol{u}}_0 + \varepsilon_2 \hat{\boldsymbol{u}}_1$ and $\bar{\boldsymbol{u}} = \bar{\boldsymbol{u}}_0 + \varepsilon_2 \bar{\boldsymbol{u}}_1$ are time-independent. For $\hat{\boldsymbol{u}}$ this is justified because the first-order flow results entirely from the oscillation, and so we expect the first-order flow to be oscillatory as well. We wish to compute the time-averaged flow at $\varepsilon_1^2 \varepsilon_2$ order and lower, and so $\bar{\boldsymbol{u}}$ can also be assumed to be time-independent.

Note that we can keep the abbreviated real part notation for linear operators.

These must satisfy

$$\text{Re}\left(\frac{\partial \boldsymbol{u}}{\partial t} + (\boldsymbol{u}\cdot\boldsymbol{\nabla})\boldsymbol{u}\right) - \boldsymbol{\nabla}^2\boldsymbol{u} = -\boldsymbol{\nabla}p, \tag{A.4}$$

$$\boldsymbol{\nabla}\cdot\boldsymbol{u} = 0, \tag{A.5}$$

$$\boldsymbol{u}(\infty) = \varepsilon_1 e^{it}\boldsymbol{x}, \tag{A.6}$$

$$\boldsymbol{u}|_{r=1} = -1\cdot\varepsilon_2\cos(2\theta - 2\Phi_1)(\boldsymbol{r}\cdot\boldsymbol{\nabla})\boldsymbol{u}\,|_{r=1}\,. \tag{A.7}$$

We obtain Equation (A.7) from Taylor expanding the near-circle from the original perfect circle. Geometrically, the radial distance from the perfect circle to the near-circle is $\varepsilon_2\cos(2\theta - 2\Phi_1)$. Thus, to a first approximation in ε_2, for $\boldsymbol{x}$ on the near-circle, $\boldsymbol{0} = \boldsymbol{u}(\boldsymbol{x}) = \boldsymbol{u}|_{r=1} + \varepsilon_2\cos(2\theta - 2\Phi_i)(\boldsymbol{r}\cdot\boldsymbol{\nabla})\boldsymbol{u}|_{r=1}$.

The first term $\text{Re}\left(\frac{\partial \boldsymbol{u}}{\partial t}\right)$ in Equation (A.4) becomes

$$\text{Re}\left(\varepsilon_1\frac{ie^{it}\hat{\boldsymbol{u}}_0 - ie^{-it}\hat{\boldsymbol{u}}_0^*}{2} + \varepsilon_1\varepsilon_2\frac{ie^{it}\hat{\boldsymbol{u}}_1 - ie^{-it}\hat{\boldsymbol{u}}_1^*}{2}\right) + \mathscr{O}(\varepsilon_2^2) + \mathscr{O}(\varepsilon_1^3). \tag{A.8}$$

The expression using the real part notation is

$$\text{Re}\left(\varepsilon_1 ie^{it}\hat{\boldsymbol{u}}_0 + \varepsilon_1\varepsilon_2 ie^{it}\hat{\boldsymbol{u}}_1\right) + \mathscr{O}(\varepsilon_2^2) + \mathscr{O}(\varepsilon_1^3). \tag{A.9}$$

The second term $\text{Re}\,(\boldsymbol{u}\cdot\boldsymbol{\nabla}\boldsymbol{u})$ (to within a factor of $\mathscr{O}(\varepsilon_1^3) + \mathscr{O}(\varepsilon_2^2)$) of Equation (A.4) becomes

$$\text{Re}\left(\varepsilon_1^2\left(\frac{e^{it}\hat{\boldsymbol{u}}_0 + e^{-it}\hat{\boldsymbol{u}}_0^*}{2} + \varepsilon_2\frac{e^{it}\hat{\boldsymbol{u}}_1 + e^{-it}\hat{\boldsymbol{u}}_1^*}{2}\right)\cdot\boldsymbol{\nabla}\left(\frac{e^{it}\hat{\boldsymbol{u}}_0 + e^{-it}\hat{\boldsymbol{u}}_0^*}{2} + \varepsilon_2\frac{e^{it}\hat{\boldsymbol{u}}_1 + e^{-it}\hat{\boldsymbol{u}}_1^*}{2}\right)\right). \tag{A.10}$$

Grouping Equation (A.10) by Fourier modes yields

$$\frac{1}{4}\,\text{Re}\left(\varepsilon_1^2\left(e^{it}(\hat{\boldsymbol{u}}_0 + \varepsilon_2\hat{\boldsymbol{u}}_1) + e^{-it}(\hat{\boldsymbol{u}}_0^* + \varepsilon_2\hat{\boldsymbol{u}}_1^*)\right)\cdot\boldsymbol{\nabla}\left(e^{it}(\hat{\boldsymbol{u}}_0 + \varepsilon_2\hat{\boldsymbol{u}}_1) + e^{-it}(\hat{\boldsymbol{u}}_0^* + \varepsilon_2\hat{\boldsymbol{u}}_1^*)\right)\right). \tag{A.11}$$

Notice that any $e^{\pm 2it}$ terms will be cancelled by coefficients of the $\varepsilon_1^2 e^{\pm 2it}$ term, but since we only wish to regard the time-averaged flow at $\varepsilon_1^2\varepsilon_2$, we can discard these terms. Then Equation (A.11) yields

$$\frac{1}{4}\,\text{Re}\left(\varepsilon_1^2\,(\hat{\boldsymbol{u}}_0 + \varepsilon_2\hat{\boldsymbol{u}}_1)\cdot\boldsymbol{\nabla}\,(\hat{\boldsymbol{u}}_0^* + \varepsilon_2\hat{\boldsymbol{u}}_1^*) + \varepsilon_1^2\,(\hat{\boldsymbol{u}}_0^* + \varepsilon_2\hat{\boldsymbol{u}}_1^*)\cdot\boldsymbol{\nabla}\,(\hat{\boldsymbol{u}}_0 + \varepsilon_2\hat{\boldsymbol{u}}_1)\right). \tag{A.12}$$

Dropping ε_2^2 terms and collapsing conjugate sums to real expressions yields

$$\frac{1}{2}\,\text{Re}\left(\varepsilon_1^2\Re(\hat{\boldsymbol{u}}_0\cdot\boldsymbol{\nabla}\hat{\boldsymbol{u}}_0) + \varepsilon_1^2\varepsilon_2\Re(\hat{\boldsymbol{u}}_0\cdot\boldsymbol{\nabla}\hat{\boldsymbol{u}}_1^* + \hat{\boldsymbol{u}}_1^*\cdot\boldsymbol{\nabla}\hat{\boldsymbol{u}}_0)\right) + \mathscr{O}(\varepsilon_1^3) + \mathscr{O}(\varepsilon_2^2). \tag{A.13}$$

Finally we can drop the $\Re$ symbol and get

$$\text{Re}\left(\frac{1}{2}\varepsilon_1^2(\hat{\boldsymbol{u}}_0\cdot\boldsymbol{\nabla}\hat{\boldsymbol{u}}_0^*) + \frac{1}{2}\varepsilon_1^2\varepsilon_2(\hat{\boldsymbol{u}}_0\cdot\boldsymbol{\nabla}\hat{\boldsymbol{u}}_1^* + \hat{\boldsymbol{u}}_1^*\cdot\boldsymbol{\nabla}\hat{\boldsymbol{u}}_0)\right) + \mathscr{O}(\varepsilon_1^3) + \mathscr{O}(\varepsilon_2^2). \tag{A.14}$$

The next term in Equation (A.4) is

$$-\boldsymbol{\nabla}^2\boldsymbol{u} = -\varepsilon_1 e^{it}\boldsymbol{\nabla}^2\hat{\boldsymbol{u}}_0 - \varepsilon_1\varepsilon_2 e^{it}\boldsymbol{\nabla}^2\hat{\boldsymbol{u}}_1 - \varepsilon_1^2\boldsymbol{\nabla}^2\bar{\boldsymbol{u}}_0 - \varepsilon_1^2\varepsilon_2\boldsymbol{\nabla}^2\bar{\boldsymbol{u}}_1 + \mathscr{O}(\varepsilon_1^3) + \mathscr{O}(\varepsilon_2^2). \tag{A.15}$$

Finally, using Equation (A.3) the right side of Equation (A.4) is

$$-\boldsymbol{\nabla}p = -\varepsilon_1 e^{it}(\boldsymbol{\nabla}\hat{p}_0 + \varepsilon_2\boldsymbol{\nabla}\hat{p}_1) - \varepsilon_1^2(\boldsymbol{\nabla}\bar{p}_0 + \varepsilon_2\boldsymbol{\nabla}\bar{p}_1) + \mathscr{O}(\varepsilon_1^3) + \mathscr{O}(\varepsilon_2^2). \tag{A.16}$$

Putting all the parts of Equation (A.4) together, the three expressions from Equation (A.9), Equation (A.14), Equation (A.15)

$$\mathrm{Re}\left(\varepsilon_1 i e^{it}\hat{\boldsymbol{u}}_0 + \varepsilon_1\varepsilon_2 i e^{it}\hat{\boldsymbol{u}}_1\right) + \mathscr{O}(\varepsilon_1^3) + \mathscr{O}(\varepsilon_2^2), \tag{A.17}$$

$$\mathrm{Re}\left(\varepsilon_1^2\frac{1}{2}(\hat{\boldsymbol{u}}_0\cdot\boldsymbol{\nabla}\hat{\boldsymbol{u}}_0) + \varepsilon_1^2\varepsilon_2\frac{1}{2}(\hat{\boldsymbol{u}}_0\cdot\boldsymbol{\nabla}\hat{\boldsymbol{u}}_1^* + \hat{\boldsymbol{u}}_1^*\cdot\boldsymbol{\nabla}\hat{\boldsymbol{u}}_0)\right) + \mathscr{O}(\varepsilon_1^3) + \mathscr{O}(\varepsilon_2^2), \tag{A.18}$$

$$-\varepsilon_1 e^{it}\boldsymbol{\nabla}^2\hat{\boldsymbol{u}}_0 - \varepsilon_1\varepsilon_2 e^{it}\boldsymbol{\nabla}^2\hat{\boldsymbol{u}}_1 - \varepsilon_1^2\boldsymbol{\nabla}^2\bar{\boldsymbol{u}}_0 - \varepsilon_1^2\varepsilon_2\boldsymbol{\nabla}^2\bar{\boldsymbol{u}}_1 + \mathscr{O}(\varepsilon_1^3) + \mathscr{O}(\varepsilon_2^2), \tag{A.19}$$

sum to equal the expression from Equation (A.16)

$$-\varepsilon_1 e^{it}(\boldsymbol{\nabla}\hat{p}_0 + \varepsilon_2\boldsymbol{\nabla}\hat{p}_1) - \varepsilon_1^2(\boldsymbol{\nabla}\bar{p}_0 + \varepsilon_2\boldsymbol{\nabla}\bar{p}_1) + \mathscr{O}(\varepsilon_1^3) + \mathscr{O}(\varepsilon_2^2). \tag{A.20}$$

We are now justified in dropping the $\mathscr{O}(\varepsilon_1^3) + \mathscr{O}(\varepsilon_2^2)$ terms.

Matching the coefficients of $\varepsilon_1, \varepsilon_1^2, \varepsilon_1\varepsilon_2, \varepsilon_1^2\varepsilon_2$ in these four expressions, yields

$$\mathrm{Re}\left(ie^{it}\hat{\boldsymbol{u}}_0\right) - e^{it}\boldsymbol{\nabla}^2\hat{\boldsymbol{u}}_0 = -e^{it}\boldsymbol{\nabla}\hat{p}_0, \tag{A.21}$$

$$\frac{1}{2}\mathrm{Re}(\hat{\boldsymbol{u}}_0\cdot\boldsymbol{\nabla}\hat{\boldsymbol{u}}_0) - \boldsymbol{\nabla}^2\bar{\boldsymbol{u}}_0 = -\boldsymbol{\nabla}\bar{p}_0, \tag{A.22}$$

$$\mathrm{Re}(ie^{it}\hat{\boldsymbol{u}}_1) - e^{it}\boldsymbol{\nabla}^2\hat{\boldsymbol{u}}_1 = -e^{it}\boldsymbol{\nabla}\hat{p}_1, \tag{A.23}$$

$$\frac{1}{2}\mathrm{Re}(\hat{\boldsymbol{u}}_0\cdot\boldsymbol{\nabla}\hat{\boldsymbol{u}}_1^* + \hat{\boldsymbol{u}}_1^*\cdot\boldsymbol{\nabla}\hat{\boldsymbol{u}}_0) - \boldsymbol{\nabla}^2\bar{\boldsymbol{u}}_1 = -\boldsymbol{\nabla}\bar{p}_1. \tag{A.24}$$

Finally, removing e^{it} we obtain

$$(\boldsymbol{\nabla}^2 - i\,\mathrm{Re})\hat{\boldsymbol{u}}_0 = \boldsymbol{\nabla}\hat{p}_0, \tag{A.25}$$

$$\boldsymbol{\nabla}^2\bar{\boldsymbol{u}}_0 = \boldsymbol{\nabla}\bar{p}_0 + \frac{1}{2}\mathrm{Re}(\hat{\boldsymbol{u}}_0\cdot\boldsymbol{\nabla}\hat{\boldsymbol{u}}_0), \tag{A.26}$$

$$(\boldsymbol{\nabla}^2 - i\,\mathrm{Re})\hat{\boldsymbol{u}}_1 = \boldsymbol{\nabla}\hat{p}_1, \tag{A.27}$$

$$\boldsymbol{\nabla}^2\bar{\boldsymbol{u}}_1 = \boldsymbol{\nabla}\bar{p}_1 + \frac{1}{2}\mathrm{Re}(\hat{\boldsymbol{u}}_0\cdot\boldsymbol{\nabla}\hat{\boldsymbol{u}}_1^* + \hat{\boldsymbol{u}}_1^*\cdot\boldsymbol{\nabla}\hat{\boldsymbol{u}}_0). \tag{A.28}$$

The other Equation (A.5) becomes

$$\boldsymbol{\nabla}\cdot\hat{\boldsymbol{u}}_0 = \boldsymbol{\nabla}\cdot\bar{\boldsymbol{u}}_0 = \boldsymbol{\nabla}\cdot\hat{\boldsymbol{u}}_1 = \boldsymbol{\nabla}\cdot\bar{\boldsymbol{u}}_1 = 0. \tag{A.29}$$

The first boundary condition Equation (A.6) becomes

$$\hat{\boldsymbol{u}}_0(\infty) = \boldsymbol{x}, \quad \bar{\boldsymbol{u}}_0(\infty) = \hat{\boldsymbol{u}}_1(\infty) = \bar{\boldsymbol{u}}_1(\infty) = 0. \tag{A.30}$$

The second boundary condition Equation (A.7) becomes

$$\varepsilon_1 e^{it}(\hat{\boldsymbol{u}}_0 + \varepsilon_2\hat{\boldsymbol{u}}_1) + \varepsilon_1^2(\bar{\boldsymbol{u}}_0 + \varepsilon_2\bar{\boldsymbol{u}}_1) = -\varepsilon_2 \cos(2\theta - 2\Phi_i)(\boldsymbol{r}\cdot\boldsymbol{\nabla})(\varepsilon_1 e^{it}(\hat{\boldsymbol{u}}_0 + \varepsilon_2\hat{\boldsymbol{u}}_1) + \varepsilon_1^2(\bar{\boldsymbol{u}}_0 + \varepsilon_2\bar{\boldsymbol{u}}_1)). \tag{A.31}$$

In Equation (A.30) and Equation (A.31), the only terms that match are $\varepsilon_1\varepsilon_2$ and $\varepsilon_1^2\varepsilon_2$, which yield

$$e^{it}\hat{\boldsymbol{u}}_1 = -\cos(2\theta - 2\Phi_i)(\boldsymbol{r}\cdot\boldsymbol{\nabla})e^{it}\hat{\boldsymbol{u}}_0, \tag{A.32}$$

$$e^{it}\bar{\boldsymbol{u}}_1 = -\cos(2\theta - 2\Phi_i)(\boldsymbol{r}\cdot\boldsymbol{\nabla})e^{it}\bar{\boldsymbol{u}}_0. \tag{A.33}$$

For the lower-order $\varepsilon_1, \varepsilon_1^2$ we obtain $\hat{\boldsymbol{u}}_0 = \hat{\boldsymbol{u}}_1 = 0$.

Reordering yields

$$\left(\boldsymbol{\nabla}^2 - i\,\mathrm{Re}\right)\hat{\boldsymbol{u}}_0 = \boldsymbol{\nabla}\hat{p}_0, \qquad \boldsymbol{\nabla}\cdot\hat{\boldsymbol{u}}_0 = 0, \tag{A.34}$$

$$\hat{\boldsymbol{u}}_0(S) = 0, \qquad \hat{\boldsymbol{u}}_0(\infty) = \boldsymbol{x}. \tag{A.35}$$

$$\boldsymbol{\nabla}^2\bar{\boldsymbol{u}}_0 = \boldsymbol{\nabla}\bar{p}_0 + \frac{1}{2}\,\mathrm{Re}\left(\hat{\boldsymbol{u}}_0\cdot\boldsymbol{\nabla}\hat{\boldsymbol{u}}_0^*\right), \qquad \boldsymbol{\nabla}\cdot\bar{\boldsymbol{u}}_0 = 0, \tag{A.36}$$

$$\bar{\boldsymbol{u}}_0(S) = 0, \qquad \bar{\boldsymbol{u}}_0(\infty) = 0. \tag{A.37}$$

$$\left(\boldsymbol{\nabla}^2 - i\,\mathrm{Re}\right)\hat{\boldsymbol{u}}_1 = \boldsymbol{\nabla}\hat{p}_1, \qquad \boldsymbol{\nabla}\cdot\hat{\boldsymbol{u}}_1 = 0, \tag{A.38}$$

$$\hat{\boldsymbol{u}}_1(S) = -\cos(2\theta - 2\Phi_i)(\boldsymbol{r}\cdot\boldsymbol{\nabla})\hat{\boldsymbol{u}}_0, \qquad \hat{\boldsymbol{u}}_1(\infty) = 0. \tag{A.39}$$

$$\boldsymbol{\nabla}^2\bar{\boldsymbol{u}}_1 = \boldsymbol{\nabla}\bar{p}_1 + \frac{1}{2}\,\mathrm{Re}\left(\hat{\boldsymbol{u}}_0\cdot\boldsymbol{\nabla}\hat{\boldsymbol{u}}_1^* + \hat{\boldsymbol{u}}_1^*\cdot\boldsymbol{\nabla}\hat{\boldsymbol{u}}_0\right), \qquad \boldsymbol{\nabla}\cdot\bar{\boldsymbol{u}}_1 = 0, \tag{A.40}$$

$$\bar{\boldsymbol{u}}_1(S) = -\cos(2\theta - 2\Phi_i)(\boldsymbol{r}\cdot\boldsymbol{\nabla})\bar{\boldsymbol{u}}_0, \qquad \bar{\boldsymbol{u}}_1(\infty) = 0. \tag{A.41}$$

Finally, we can rewrite Equations (A.36) and (A.40) using the Reynolds stresses $\boldsymbol{R}_0, R_1$ in the form $\boldsymbol{\nabla}^2\boldsymbol{u} = \boldsymbol{\nabla}p - \boldsymbol{\nabla}\cdot\boldsymbol{R}$, where $\boldsymbol{R}$ is a tensor field. Specifically, using $\boldsymbol{R}_0 = -\frac{1}{2}\,\mathrm{Re}\,\hat{\boldsymbol{u}}_0\otimes\hat{\boldsymbol{u}}_0^*$ and $\boldsymbol{R}_1 = -\frac{1}{2}\,\mathrm{Re}\,\hat{\boldsymbol{u}}_0\otimes\hat{\boldsymbol{u}}_1^*$ yields Equations (2.7) and (2.9).

Appendix B. Torque and Force Expression Derivation

For ease of notation, we adopt a coordinate system centered at O_1, the center of the first circle. Then $\boldsymbol{n} = \boldsymbol{x}$. The force vector $\boldsymbol{F}_1$ can be expressed as

$$\boldsymbol{F}_1 = \int_{\partial\Omega_1} (p\boldsymbol{I} + \frac{1}{2}\left(\boldsymbol{\nabla u} + (\boldsymbol{\nabla u})^T\right)) \cdot \boldsymbol{x}\, dS \tag{B.1}$$

$$= \int_{\partial\Omega_1} p\boldsymbol{x} + \frac{1}{2}(\boldsymbol{\nabla u}) \cdot \boldsymbol{x} + \frac{1}{2}(\boldsymbol{\nabla u})^T \cdot \boldsymbol{x}\, dS. \tag{B.2}$$

(B.3)

For the torque T_1, instead of using the cross product, we use a dot product with a modified $= \langle -y, x\rangle$ where x, y are the scalar components of $\boldsymbol{x}$. Then

$$T_1 = \int_{\partial\Omega_1} \boldsymbol{m} \cdot ((p\boldsymbol{I} + \frac{1}{2}\left(\boldsymbol{\nabla u} + (\boldsymbol{\nabla u})^T\right)) \cdot \boldsymbol{x})\, dS \tag{B.4}$$

$$= \int_{\partial\Omega_1} p\boldsymbol{m} \cdot \boldsymbol{x} + \frac{1}{2}\boldsymbol{m} \cdot \boldsymbol{\nabla u} \cdot \boldsymbol{x} + \frac{1}{2}\boldsymbol{m} \cdot (\boldsymbol{\nabla u})^T \cdot \boldsymbol{x}\, dS. \tag{B.5}$$

(B.6)

These expressions were computed by explicitly integrating across the discretized boundary $\partial\Omega_1$. Computations for $\boldsymbol{F}_2$ and T_2 are analogous.

Appendix C. Convergence

C.1. **Single-ellipse convergence.** Using $\mathrm{Re} = 10$, convergence tests for element width and domain size were conducted on all four flows $\hat{\boldsymbol{u}}_0, \bar{\boldsymbol{u}}_0, \hat{\boldsymbol{u}}_1, \bar{\boldsymbol{u}}_1$.

A reference solution $\boldsymbol{u}$, along with its corresponding four vector fields for velocity and four scalar fields for pressure, was defined using the numerical fields generated by a grid with 61,660 nodes and 2 DOFs each, with a minimum element size of 0.03. For various coarser meshes with proportional element sizes to this reference solution, the L_2 error of all eight velocity fields and pressure fields of the corresponding solutions are computed relative to the reference solution, and plotted in Figure 12a as a function of the minimum element size. The L_2 error w.r.t. element width exhibits a rate of convergence faster than the quadratic lines shown in the log-log plot, as desired. Furthermore, the L_2 error near the circles w.r.t. domain size converges faster than exponentially, as seen by the concave log-scaled plot in Figure 12b.

C.2. **Double-ellipse convergence.** Using $\mathrm{Re} = 10$, $\varphi = \frac{\pi}{2}$ and $K = 1$, we conducted similar convergence tests for all four flows. The results are seen in Figure 13, with similar discussion and results.

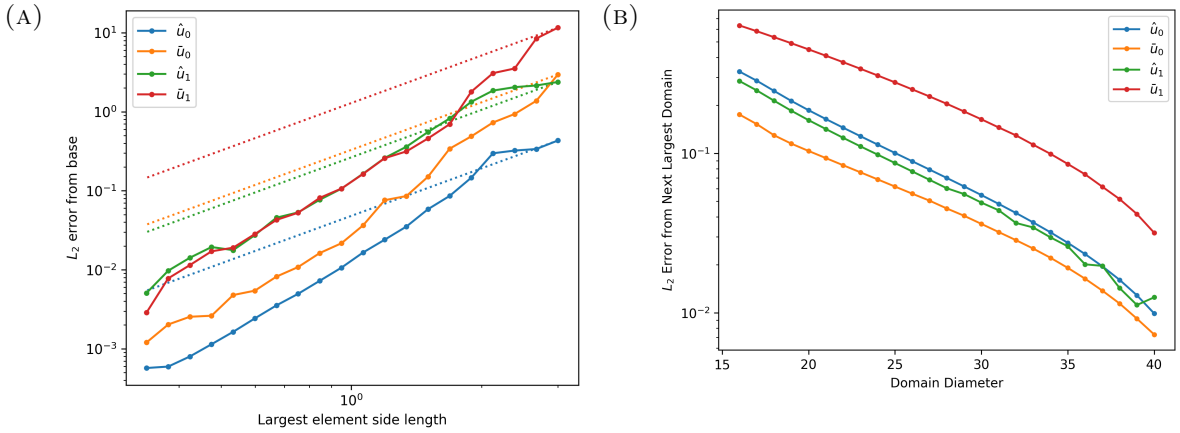

FIGURE 12. The left-hand plot is a log-log plot of L_2 error between a reference solution on the finest single-ellipse mesh and various solutions on meshes with proportional element sizes, plotted relative to the largest element size on the solution mesh. The errors are plotted for all eight velocity and pressure fields. Dashed lines denote quadratic rates of convergence. The right-hand plot is a log-scaled plot of L_2 error between a reference solution on the largest mesh and various solutions on smaller meshes, restricted to the domain with diameter 16 centered at O.

REFERENCES

1. RS Alassar and HM Badr, *Oscillating flow over oblate spheroids*, Acta mechanica **137** (1999), no. 3-4, 237–254.
2. Hugh Maurice Blackburn, *Mass and momentum transport from a sphere in steady and oscillatory flows*, Physics of fluids **14** (2002), no. 11, 3997–4011.
3. Rahul Chhabra, Jaswinder Sharma, Yan Liu, Sherri Rinker, and Hao Yan, *Dna self-assembly for nanomedicine*, Advanced drug delivery reviews **62** (2010), no. 6, 617–625.
4. S. Childress, *Mechanics of swimming and flying*, Cambridge University Press, 1981.
5. Nicholas J. Derr, Thomas Dombrowski, Chris H. Rycroft, and Daphne Klotsa, *Reciprocal swimming at intermediate reynolds number*, Journal of Fluid Mechanics **952** (2022), A8.
6. L Durlofsky and JF Brady, *Analysis of the brinkman equation as a model for flow in porous media*, Physics of Fluids **30** (1987), no. 11, 3329–3341.
7. David Fabre, Javeria Jalal, Justin S Leontini, and Richard Manasseh, *Acoustic streaming and the induced forces between two spheres*, Journal of Fluid Mechanics **810** (2017), 378–391.
8. BU Felderhof and RB Jones, *Inertial effects in small-amplitude swimming of a finite body*, Physica A: Statistical Mechanics and its Applications **202** (1994), no. 1-2, 94–118.
9. Mattia Gazzola, Médéric Argentina, and Lakshminarayanan Mahadevan, *Scaling macroscopic aquatic locomotion*, Nature Physics **10** (2014), no. 10, 758–761.
10. Geuzaine, Christophe and Remacle, Jean-Francois, *Gmsh*.
11. D. Klotsa, Michael R. Swift, R. M. Bowley, and P. J. King, *Chain formation of spheres in oscillatory fluid flows*, Physical Review E **79** (2009), no. 2, 021302.

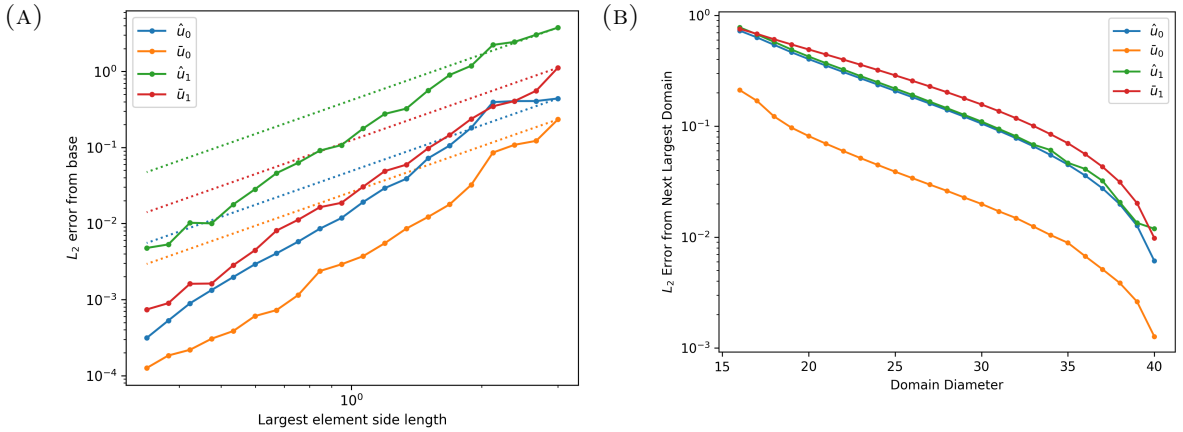

FIGURE 13. The left-hand plot is a log-log plot of L_2 error between a reference solution on the finest double-ellipse mesh and various solutions on meshes with proportional element sizes, plotted relative to the largest element size on the solution mesh. The errors are plotted for all eight velocity and pressure fields. Dashed lines denote quadratic rates of convergence. The right-hand plot is a log-scaled plot of L_2 error between a reference solution on the largest mesh and various solutions on smaller meshes, restricted to the domain with diameter 16 centered at O.

12. D Klotsa, Michael R Swift, RM Bowley, and PJ King, *Interaction of spheres in oscillatory fluid flows*, Physical Review E **76** (2007), no. 5, 056314.
13. A. Logg and G. N. Wells, *DOLFIN: automated finite element computing*, ACM Transactions on Mathematical Software **37** (2010), no. 2, 1–28.
14. A. Logg, G. N. Wells, and J. Hake, *DOLFIN: a C++/Python finite element library*, Automated Solution of Differential Equations by the Finite Element Method (A. Logg, K.-A. Mardal, and G. N. Wells, eds.), Lecture Notes in Computational Science and Engineering, vol. 84, Springer, 2012, pp. 173–225.
15. A. Logg, K. B. Ølgaard, M. E. Rognes, and G. N. Wells, *FFC: the FEniCS form compiler*, Automated Solution of Differential Equations by the Finite Element Method (A. Logg, K.-A. Mardal, and G. N. Wells, eds.), Lecture Notes in Computational Science and Engineering, vol. 84, Springer, 2012.
16. Anders Logg, Kent-Andre Mardal, and Garth Wells, *Automated solution of differential equations by the finite element method: The fenics book*, vol. 84, Springer Science & Business Media, 2012.
17. Werner Nachtigall, *Some aspects of reynolds number effects in animals*, Mathematical Methods in the applied sciences **24** (2001), no. 17-18, 1401–1408.
18. Florian Otto, Emmalee K Riegler, and Greg A Voth, *Measurements of the steady streaming flow around oscillating spheres using three dimensional particle tracking velocimetry*, Physics of fluids **20** (2008), no. 9.
19. Timothy J Pedley, *Spherical squirmers: models for swimming micro-organisms*, IMA Journal of Applied Mathematics **81** (2016), no. 3, 488–521.
20. Edward M Purcell, *Life at low reynolds number*, American journal of physics **45** (1977), no. 1, 3–11.

21. N Riley, *On a sphere oscillating in a viscous fluid*, The Quarterly Journal of Mechanics and Applied Mathematics **19** (1966), no. 4, 461–472.
22. Norman Riley, *Steady streaming*, Annual review of fluid mechanics **33** (2001), no. 1, 43–65.
23. Geoffrey Ingram Taylor, *Analysis of the swimming of microscopic organisms*, Proceedings of the Royal Society of London. Series A. Mathematical and Physical Sciences **209** (1951), no. 1099, 447–461.
24. Greg A Voth, B Bigger, MR Buckley, W Losert, MP Brenner, Howard A Stone, and JP Gollub, *Ordered clusters and dynamical states of particles in a vibrated fluid*, Physical review letters **88** (2002), no. 23, 234301.
25. Brady Wu, Bryan VanSaders, Melody X Lim, and Heinrich M Jaeger, *Hydrodynamic coupling melts acoustically levitated crystalline rafts*, Proceedings of the National Academy of Sciences **120** (2023), no. 29, e2301625120.
26. Régis Wunenburger, V Carrier, and Yves Garrabos, *Periodic order induced by horizontal vibrations in a two-dimensional assembly of heavy beads in water*, Physics of Fluids **14** (2002), no. 7, 2350–2359.

Email address: alexzhao.mailbox@gmail.com